

Gamma-ray heartbeat powered by the microquasar SS 433

Jian Li^{1†}, Diego F. Torres^{2,3,4}, Ruo-Yu Liu^{5,6}, Matthew Kerr⁷, Emma de Oña Wilhelmi^{1,2}, & Yang Su⁸

¹*Deutsches Elektronen-Synchrotron DESY, D-15738 Zeuthen, Germany* [†]jian.li@desy.de

²*Institute of Space Sciences (ICE, CSIC), Campus UAB, Carrer de Magrans s/n, 08193 Barcelona, Spain*

³*Institució Catalana de Recerca i Estudis Avançats (ICREA), E-08010 Barcelona, Spain*

⁴*Institut d'Estudis Espacials de Catalunya (IEEC), 08034 Barcelona, Spain*

⁵*School of Astronomy and Space Science, Nanjing University, Nanjing, China*

⁶*Key Laboratory of Modern Astronomy and Astrophysics (Nanjing University), Ministry of Education, Nanjing, China*

⁷*Space Science Division, Naval Research Laboratory, Washington, DC 20375, USA*

⁸*Purple Mountain Observatory and Key Laboratory of Radio Astronomy, Chinese Academy of Sciences, Nanjing 210034, China*

Microquasars, the local siblings of extragalactic quasars, are binary systems comprising a compact object and a companion star. By accreting matter from their companions, microquasars launch powerful winds and jets, influencing the interstellar environment around them. Steady gamma-ray emission is expected to rise from their central objects, or from

interactions between their outflows and the surrounding medium. The latter prediction was recently confirmed with the detection of SS 433¹ at high (TeV) energies. In this report, we analyze more than ten years of GeV gamma-ray data from the *Fermi* Gamma-ray Space Telescope on this source. Detailed scrutiny of the data reveal emission in the SS 433 vicinity, co-spatial with a gas enhancement, and hints for emission possibly associated with a terminal lobe of one of the jets. Both gamma-ray excesses are relatively far from the central binary, and the former shows evidence for a periodic variation at the precessional period of SS 433, linking it with the microquasar. This result challenges obvious interpretations and is unexpected from any previously published theoretical models. It provides us with a chance to unveil the particle transport from SS 433 and to probe the structure of the local magnetic field in its vicinity.

SS 433 is a unique Galactic microquasar containing a compact object, most likely a black hole of $\sim 10\text{--}20\ M_{\odot}$ orbiting a $\sim 30\ M_{\odot}$ A3-7 supergiant star with an orbital period of 13.082 days². The rate of mass transfer from the companion is determined from the analysis of optical lines³ and is thought to be as high as $10^{-4}\ M_{\odot}\ \text{yr}^{-1}$, which is orders of magnitude larger than the Eddington limit. This steady super-critical accretion state powers highly collimated jets of plasma and mass-loaded non-polar outflows at a similar level⁴⁻⁶, with kinetic powers exceeding $\gtrsim 10^{39}\ \text{erg}\ \text{s}^{-1}$. The jets appear to inflate the W50 nebula surrounding SS 433⁷, and perhaps also the H I shell-like structure seen on an even larger scale⁸. Jets and outflows in SS 433 eject matter at relativistic speeds, $\sim 0.2c$ ^{6,9}, while precessing with a period of 162.250 days¹⁰. This timing signature is ex-

plained by the periodic pull of the giant secondary star, moving the accretion disk and its outflows in solidarity. Doppler shifts of H and He lines in the optical as well as of highly ionized Fe lines in the X-rays indicate relativistic baryon content in the jets^{9,11}; whereas knots seen at radio frequency indicate the existence of relativistic electrons¹².

Synchrotron emission in radio and X-ray bands is observed from the jet termination lobes^{7,13}. Recently, very high energy gamma rays (> 25 TeV) were also observed at these positions by HAWC, with a likely origin from inverse-Compton scattering between locally-accelerated electrons and cosmic microwave background radiation¹. GeV emission would also be expected from the same leptonic processes at the lobes of SS 433, although at a level that would be challenging to detect with the *Fermi*-Large Area Telescope (LAT)¹. Nonetheless, the existence of baryons in the jets has also promoted models in which gamma-ray emission can rise hadronically at the jet base (see, e.g.,¹⁴), and/or in interactions between molecular clouds and cosmic rays that diffuse away from the accelerating region (see, e.g.,¹⁵). We come back to these ideas below, in the context of our findings.

Searches for GeV emission from SS 433 have thus been a subject of strong interest, and a number of studies using *Fermi*-LAT data have arrived at inconsistent conclusions^{16–19}. However, as we detail in the *Methods* section, these studies lacked a proper treatment for the contamination produced from nearby sources, in particular from the pulsar PSR J1907+0602, and are thus at risk of systematic biases.

Using 10.5 years of *Fermi*-LAT data, we carried out a deep search for gamma-ray emission related to SS 433 in the 100 MeV – 300 GeV band during the off-peak phase of PSR J1907+0602. Full details of our search are described in the *Methods* section. We detected two GeV excesses near SS 433, neither at the position of the central compact object. These excesses are shown in Figure 1 (top panel), together with the radio morphology of the W50 nebula and X-ray contours of the lobes. There is a GeV excess (hereafter referred to as Fermi J1913+0515, at R.A. = $288.28^\circ \pm 0.04^\circ$, decl. = $5.27^\circ \pm 0.04^\circ$) that lies adjacent to the X-ray contours of the SS 433 east lobe but does not overlap with them. Fermi J1913+0515 is spatially consistent with the *Fermi*-LAT 8-year Point Source List (FL8Y) gamma-ray source FL8Y J1913.3+0515. No gamma-ray source is found at this location in the *Fermi* Large Area Telescope Fourth Source Catalog (4FGL; see *Methods*). Assuming a power-law spectral shape ($dN/dE = N_0(E/E_0)^{-\Gamma} \text{ cm}^{-2} \text{ s}^{-1} \text{ MeV}^{-1}$), Fermi J1913+0515 is detected with a Test Statistic (TS) value of 39 (notionally 5.9σ) and a spectral index of $2.39 \pm 0.10_{\text{stat}} \pm 0.05_{\text{sys}}$, yielding an energy flux of $(1.25 \pm 0.24_{\text{stat}} \pm 0.39_{\text{sys}}) \times 10^{-11} \text{ erg cm}^{-2} \text{ s}^{-1}$, corresponding to a luminosity of $3.2 \times 10^{34} \text{ erg s}^{-1}$ ($d = 4.6 \text{ kpc}^{20}$). No morphological extension nor spectral cutoff can be identified (see *Methods*).

The GeV excess in the west is spatially coincident with the west lobe of SS 433, and is located at R.A. = $287.46^\circ \pm 0.09^\circ$, decl. = $4.98^\circ \pm 0.08^\circ$. Assuming a power-law spectral shape, the likelihood analysis of the excess results in a TS value of 15 (notionally 3.5σ), which is below the formal source detection threshold (TS=25, see *Methods*). This dim west excess has a spectral index of $2.30 \pm 0.16_{\text{stat}} \pm 0.11_{\text{sys}}$ and an energy flux of $(0.75 \pm 0.25_{\text{stat}} \pm 0.41_{\text{sys}}) \times 10^{-11} \text{ erg cm}^{-2} \text{ s}^{-1}$.

In an attempt to explore whether these excesses are linked to SS 433, we produced exposure-corrected, weighted 1-day light curves above 1 GeV (see *Methods*) and searched for timing signals at the orbital and precessional period. Using Lomb-Scargle timing analysis, a hint of a periodic signal at 160.88 ± 2.66 days is detected from Fermi J1913+0515 with a single-frequency significance of 3.6σ and a false alarm probability of 3.7×10^{-3} (see *Methods*). This period is consistent with the jet precession period of 162.250 days (Figure 2). Neither the west excess nor other sources in the vicinity show the same periodicity, and none of the sources indicates variability at the orbital period. Fermi J1913+0515 itself is significantly detected, with a TS value of 31 (5.2σ) above 1 GeV. Thus, guided by the hint of precessional variability, we carried out a likelihood analysis in two broad precession phases, 0.0–0.5 and 0.5–1.0 above 1 GeV, adopting the SS 433 ephemeris of reference (T_0 (JD) = 2443508.4098, see *Methods*)¹⁰. The difference is marked: Fermi J1913+0515 is significantly detected in the precession phase interval 0.0–0.5 with a TS value of 39 (5.9σ) and not detected at all in the precession phase interval 0.5–1.0, yielding a TS value of 3 (1σ , Figure 3, top panel). The precessional phase light curve is shown in Figure 3, bottom panel. Through likelihood analysis, we see that the flux in the precessional phase interval 0.0–0.5 is significantly higher than that in precession phase interval 0.5–1.0 at the 4.2σ level. The fluxes between the two precessional phase intervals significantly deviate from a constant at a 3.5σ level (see *Methods*).

The location of Fermi J1913+0515 and the west excess nearby SS 433 reported here argues for possible physical connections. On the one hand, the 95% confidence level position circle of the west excess covers the X-ray excess¹³ and is close to the recent multi-TeV source detected by

HAWC, for which a leptonic, locally-accelerated origin was energetically preferred¹. On the other hand, the adjacent position, the 160.88 ± 2.66 -days timing signal and its related flux variability link Fermi J1913+0515 to the microquasar SS 433. However, this connection poses a significant interpretation challenge: Which is the mechanism powering the GeV emission? How is this periodic signal generated?

Detectable gamma-ray signals from SS 433 and other microquasars have been predicted in the past, even at a roughly compatible level to the sources described here^{14,21,22}. Moreover, due to the precessional period of SS 433, a periodicity in the emission of GeV photons has also been predicted¹⁴. This signal was proposed to originate in the periodically varying –along with the precessional movement– gamma-ray absorption due to interactions with matter (via γN) and fields (via $\gamma\gamma$ processes) of the disk and the star²³. In this scenario, the dominant gamma-ray production channel is hadronic, and emission must happen at the very base of the jets, at sufficiently high ambient densities so that pp interactions can proceed. Since the same proton population would also generate copious freely-escaping neutrinos, the lack of a detected neutrino source at the position of SS 433²⁴ requires that the model parameters be calibrated such that they allow both a detectable signal in gamma rays and a non-detectable neutrino flux²⁵. This is slightly complicated by the fact that the relativistic proton distribution derived in¹⁴ has been later revised²⁶, leading to deviations for the assumed proton fluxes for jets displaying large Lorentz factors and/or small viewing angles. The latest H.E.S.S. and MAGIC upper limits²⁷ on the central source would require that the fractional power carried by relativistic protons in the SS 433 jets be $\leq 10^{-5}$. Future observations

with the next generation of gamma-ray and neutrino detectors will assess this possibility further. However, due to the significant positional offset between the predicted and the detected source (~ 35 pc away from the central source, at a distance of ~ 4.6 kpc²⁰), we can already conclude that the periodicity reported for Fermi J1913+0515 cannot be related to such gamma-ray absorption.

Coincident in position with Fermi J1913+0515 and at the consistent distance as SS 433, there is a gas enhancement beyond the diffuse average (Figure 1, bottom panel). The gas excess is located within a projected region of $R_c \sim 20$ pc, with a mass that can reach up to $M \sim 25000$ M_\odot (see *Methods*). Assuming a spherical region of radius R_c , the average density is $n \sim 22$ cm⁻³, although can be lower if the mass is more extended perpendicular to the plane of the sky.

Direct periodic illumination of such region by the eastern jet seems unlikely. On the one hand, the coherence of the radio jet appears to be sustained on the arcsecond scale only²⁸. Simulations confirm that the jet loses the helical morphology after a few precession cycles, due to the interaction with the surrounding medium²⁹. On the other hand, Fermi J1913+0515 is not located within the extrapolated jet cone.

The interaction of protons accelerated in the central region of microquasars or at the jet termination in neighboring clouds has been studied in the past¹⁵. In such scenarios, protons diffuse from their injection point and produce hadronic gamma-rays when finding appropriate targets. The average level of gamma-ray flux we measure from Fermi J1913+0515 can be accommodated in this setting. This scenario, however, can hardly explain the periodicity. Even assuming a periodic,

impulsive injection of cosmic rays containing most of the jet energy released in a single period, these injections would not be energetically relevant individually, providing a cosmic-ray density subdominant to the Galactic sea. The *Methods* section gives further details on these considerations.

An alternative possibility for proton injection could be provided by the relativistic equatorial outflow recently characterized by *NuSTAR*⁶: This outflow has a more favorable geometry with respect to the gas enhancement. The line-of-sight outflow velocity is 0.14–0.29c (potentially higher if we are not viewing along the direction of the outflow), and it even exceeds the velocities seen in the approaching jet ejecta at any precessional phase⁶. Energetically, the outflow is as powerful as that of the jet and is believed to precess in solidarity with the jet and the accretion disk. The screening of the central source by these outflows would explain why SS 433 is not as X-ray bright as the $10^{-4} \text{ M}_{\odot} \text{ yr}^{-1}$ accretion rate would indicate⁶.

However, and similarly to what was noted above, in order to have proton interactions associated with the precessional periodicity, protons should arrive at a cloud periodically at a sufficient rate to produce the gamma-ray emission level seen. Anisotropic diffusion³⁰ or streaming of cosmic rays along a flux tube could perhaps help: In anisotropic diffusion, the cosmic-ray density along the tube, at a generic distance R_t from the source, would be proportional to³⁰ $n \propto (R_t R_{src}^2)^{-1}$ instead of R_t^{-3} as in the isotropic case (where R_{src} is the typical scale for the accelerating region, which for SS 433 can be much smaller than 1 pc). If the gas enhancement and SS 433 are periodically connected via a magnetic flux tube within the W50 nebula, or if the very injection at the base of

the magnetic tube is periodic, a sufficient number of protons could arrive and interact at the cloud in each period. In this scenario, most of the accelerated protons in one period, i.e., a reservoir up to 4×10^{45} erg, considering a kinetic luminosity of 3×10^{39} erg s⁻¹ and 10% of it converting to cosmic rays, might be assumed to reach the region of interest, which eases the energetic requirements. Maintaining periodic coherence, however, requires cosmic rays being funnelled into the gas enhancement and interacting in a small clump or cusp of density (in what otherwise is a relatively low-density gas enhancement, see *Methods*). Thus, this is a priori unlikely too, although further studies are required to rule it out. The periodic variability is intriguing, and difficult to reconcile with our current understanding of the source environment under common lore interpretations.

SS 433 continues to amaze observers at all frequencies and theoreticians alike, and is certain to provide a testbed for our ideas on cosmic-ray production and propagation near microquasars for years to come.

Acknowledgments

The *Fermi* LAT Collaboration acknowledges generous ongoing support from a number of agencies and institutes that have supported both the development and the operation of the LAT as well as scientific data analysis. These include the National Aeronautics and Space Administration and the Department of Energy in the United States, the Commissariat à l’Energie Atomique and the Centre National de la Recherche Scientifique / Institut National de Physique Nucléaire et de

Physique des Particules in France, the Agenzia Spaziale Italiana and the Istituto Nazionale di Fisica Nucleare in Italy, the Ministry of Education, Culture, Sports, Science and Technology (MEXT), High Energy Accelerator Research Organization (KEK) and Japan Aerospace Exploration Agency (JAXA) in Japan, and the K. A. Wallenberg Foundation, the Swedish Research Council and the Swedish National Space Board in Sweden. Additional support for science analysis during the operations phase is gratefully acknowledged from the Istituto Nazionale di Astrofisica in Italy and the Centre National d'Études Spatiales in France. This work performed in part under DOE Contract DE-AC02-76SF00515.

This publication utilizes data from Galactic ALFA HI (GALFA HI) survey data set obtained with the Arecibo L-band Feed Array (ALFA) on the Arecibo 305m telescope. The Arecibo Observatory is operated by SRI International under a cooperative agreement with the National Science Foundation (AST-1100968), and in alliance with Ana G. Méndez-Universidad Metropolitana, and the Universities Space Research Association. The GALFA HI surveys have been funded by the NSF through grants to Columbia University, the University of Wisconsin, and the University of California.

J. L. acknowledges the support from the Alexander von Humboldt Foundation and the National Natural Science Foundation of China via NSFC-11673013, NSFC-11733009. The work of D. F. T. has been supported by the grants PGC2018-095512-B-I00, SGR2017-1383, and AYA2017-92402-EXP. J. L. and D. F. T. acknowledge the fruitful discussions with the international team on

“Understanding and unifying the gamma rays emitting scenarios in high mass and low mass X-ray binaries” of the ISSI (International Space Science Institute), Beijing, as well as the support of the PHAROS COST Action (CA16214). E.O.W acknowledges the support from the Alexander von Humboldt Foundation. Work at NRL is supported by NASA. We thank Dr. Rolf Bühler, Dr. Fabio Acero, Dr. Jean Ballet, Dr. Philippe Bruel, Dr. David J. Thompson, Dr. Seth Digel and Dr. Guðlaugur Jóhannesson for their insightful comments and helpful suggestions. We thank Dr. Peng Zhang for the help with Weighted Wavelet Z-transform.

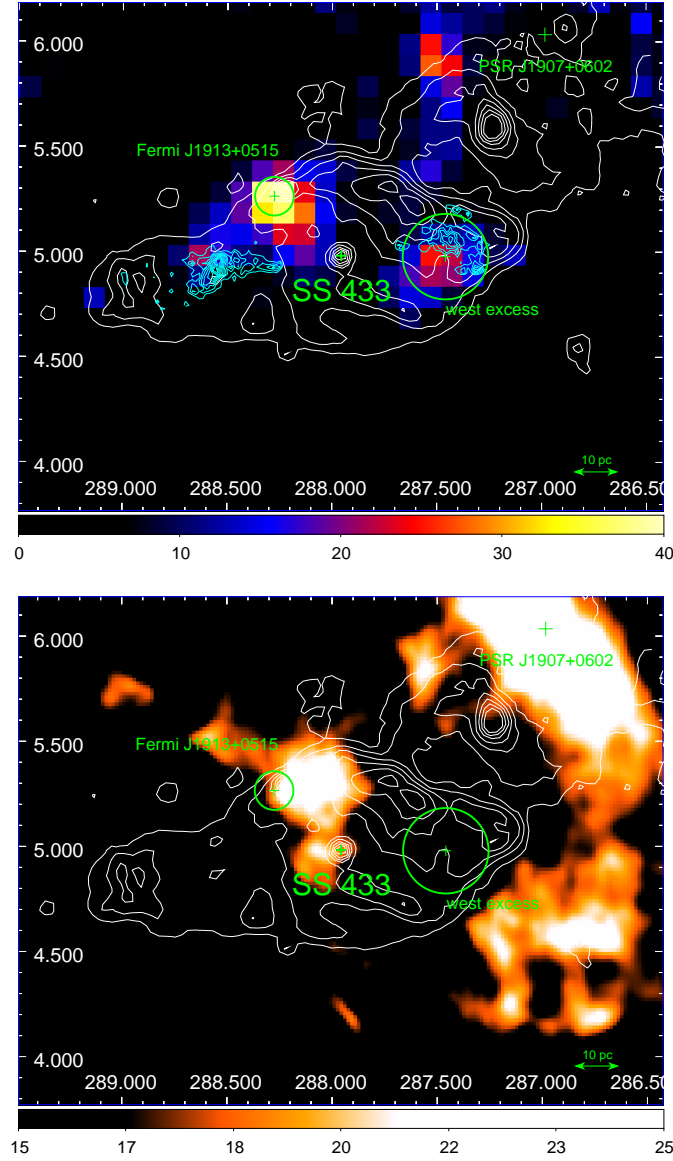


Figure 1: Gamma-ray and atomic cloud images of the SS 433 region. **Top:** *Fermi*-LAT TS map of SS 433 region in 0.1–300 GeV during the off-peak phase of PSR J1907+0602. Background sources have been modelled and subtracted (see *Methods*). The color scale shows the Test Statistic (*TS*), the square root of which gives an approximate detection significance. The 95% confidence level circle of the positions of Fermi J1913+0515 and west excess are shown in green. The white contours show the radio continuum emission from the Effelsberg 11 cm survey. Cyan contours show the X-ray emission measured by ROSAT. **Bottom:** Arecibo H I emission integrated in the interval 65–82 km s^{−1} in units of K km/s. The image has been scaled by $\sin |b|$ (b is Galactic latitude) to enhance the features far from the Galactic plane⁸. The x and y axes are R.A. and decl. (J2000, degrees).

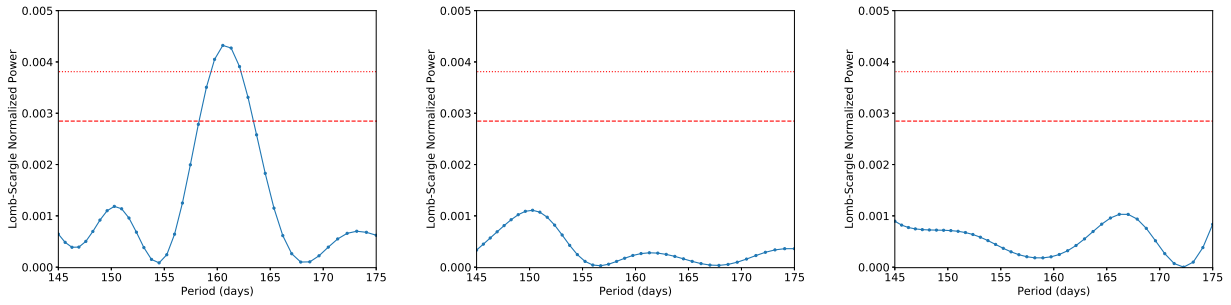


Figure 2: SS 433 precession signal seen in Fermi J1913+0515. Exposure-corrected Lomb-Scargle power spectra constructed from the 1–300 GeV weighted light curve of Fermi J1913+0515, the west excess, and PSR J1907+0602. The red dotted and dashed line indicates false alarm probability of 1% and 5% level. Only Fermi J1913+0515 shows a significant hint for the detection of the precessional period, which is confirmed by likelihood analysis.

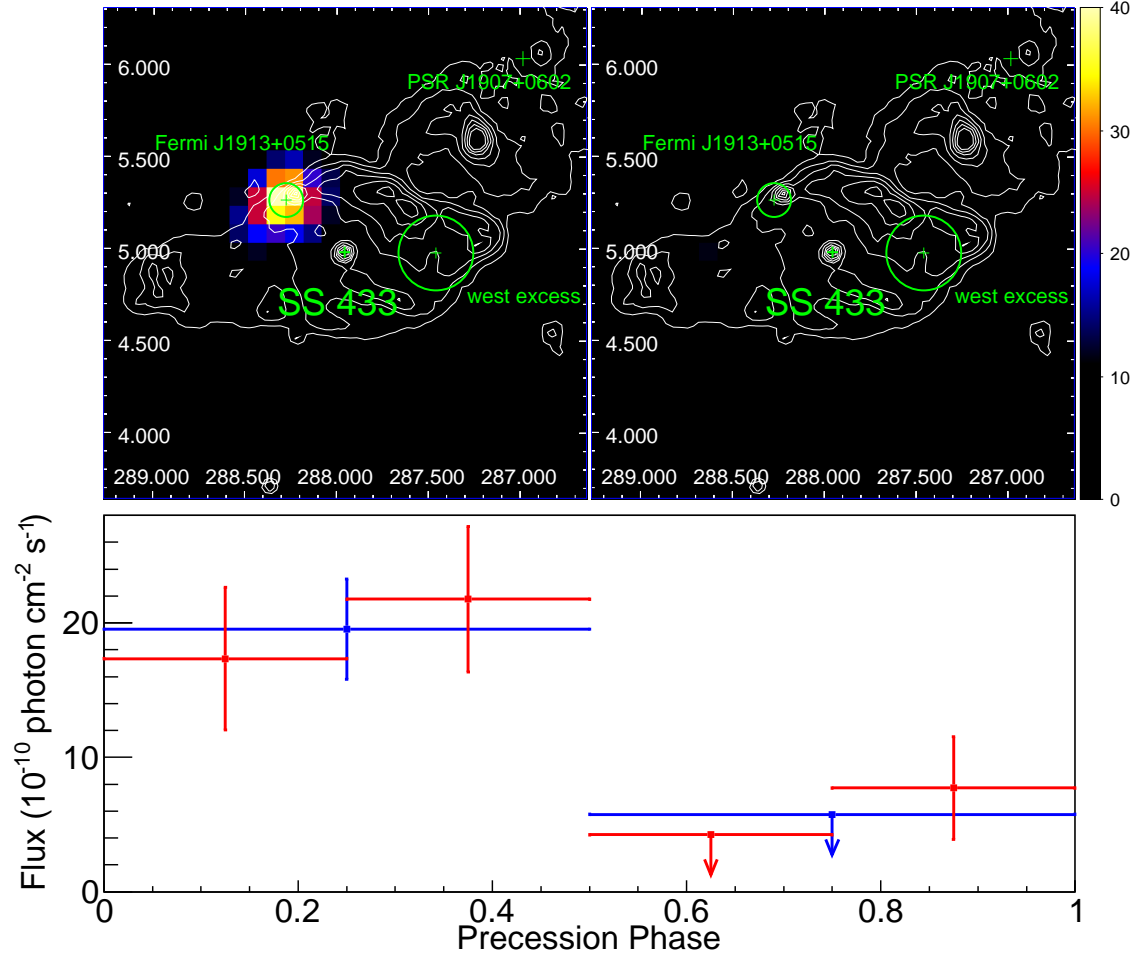


Figure 3: Analysis of *Fermi*-LAT data in precessional phases 0.0–0.5 (left) and 0.5–1.0 (right).

Top: TS map of the SS 433 region in the 1–300 GeV band for the precessional phases 0.0–0.5 (left) and 0.5–1.0 (right). The contours and labels are as in Figure 1. **Bottom:** Precessional phase light curve of Fermi J1913+0515 in 1–300 GeV with a binning of 0.5 (blue) and 0.25 (red). The upper limits are at the 95% confidence level.

Methods

Details on the *Fermi*-LAT data analysis

The analysis shown in this paper uses 10.5 years of *Fermi*-LAT³¹ data, from 2008 August 4 (MJD 54682) to 2019 January 28 (MJD 58511). We have considered all events with reconstructed energies between 100 MeV–300 GeV and positions within a circular region of interest (ROI) of 15° radius centered on PSR J1907+0602. We selected photons of the “Pass 8” event class, using *Fermi* Science Tools³² 11-07-00 release.

We have used the “P8R3 V2 Source” instrument response functions (IRFs), adopting a zenith angle threshold of $< 90^\circ$ to reject contaminating gamma rays from the Earth’s limb. A spectral-spatial model was constructed from the *Fermi* Large Area Telescope Fourth Source Catalog (4FGL)³³. Both Galactic (“gll_iem_v07.fits”) as well as isotropic diffuse emission components (“iso_P8R3_SOURCE_V2_v1.txt”³⁴) and known gamma-ray sources within 20° of PSR J1907+0602 were included.

The spectral parameters of the sources within 4° of our target were left free while those of other (farther) sources included were fixed at the 4FGL values. The spectral analysis was performed using a binned maximum likelihood fit (spatial bin size 0.1 degree, AIT projection and 30 logarithmically spaced bins in the 0.1–300 GeV range) with the Science Tool *gtlike*. The significance of the sources were evaluated by the Test Statistic (TS). This statistic is defined as

$TS = -2 \ln(L_{max,0}/L_{max,1})$, where $L_{max,0}$ is the maximum likelihood value for a model in which the source studied is removed (the “null hypothesis”), and $L_{max,1}$ is the corresponding maximum likelihood value with this source being incorporated. The larger the value of TS, the less likely it is that the null hypothesis (no source) is correct, and that instead a significant gamma-ray excess lies at the tested position. For nested models with nondegenerate parameters, \sqrt{TS} is approximately equal to the detection significance in σ of a given source. A TS of 25 is adopted as the detection threshold in this paper, as is similarly done in the *Fermi*-LAT source catalogs³⁵.

The extension significance was defined as $TS_{ext} = -2 \ln(L_{point}/L_{ext})$, where L_{ext} and L_{point} are the *gtlike* global likelihood of the extended source hypotheses and the point source, respectively. A threshold for claiming the source to be spatially extended is set as $TS_{ext} > 16$, which corresponds to a significance of $\sim 4\sigma$. The *Fermipy* python package³⁶ was used to produce the TS maps and source localizations in this paper. Energy dispersion correction has been applied in the analysis.

The systematic errors have been estimated following standard procedures, i.e., by repeating the analysis using modified IRFs³⁷ that bracket the effective area³⁸, and artificially changing the normalization of the Galactic diffuse model by $\pm 6\%$ ³⁹. The latter dominates the systematic errors. In this paper, the first (second) uncertainty shown corresponds to the statistical (systematic) error.

Pulsar contamination and the need of gating

PSR J1907+0602 is a bright gamma-ray pulsar located only 1.4° away from SS 433. The

photons from PSR J1907+0602 dominate the emission of the SS 433 region (Figure 4), up to the point that Fermi J1913+0515 is not visible in the counts map. To produce the pulse profile, we selected photons from PSR J1907+0602 above 300 MeV within a radius of 0.6° , selections which maximized the H-test statistic^{40,41}.

We have assigned pulsar rotational phases for each gamma-ray photon that passed the selection criteria, applying an updated ephemeris for PSR J1907+0602 and using *Tempo2*⁴² with the *Fermi* plug-in⁴³. The pulsation from PSR J1907+0602 is significantly detected with an H-Test value of 14948 ($m=20$). Its pulse profile is shown in Figure 4, right panel.

To check for the level of contamination at the SS 433 region that may be produced by PSR J1907+0602, we extracted photons above 100 MeV within a radius of 0.6° centered on SS 433 (dashed circle in Figure 4, left panel), thus covering both regions of interest for this work, Fermi J1913+0515 and the west excess. Pulsar rotational phases for each gamma-ray photon were calculated at that position using the ephemeris of the pulsar PSR J1907+0602. The folded profile is shown in Figure 4, right panel. It shows that the pulsation of PSR J1907+0602 is significantly recovered at the position of interest, with an H-Test value of 418 ($m=11$, above 8σ). This exercise demonstrates that a non-gated analysis of the gamma-ray photons at the position of SS 433 is severely contaminated by PSR J1907+0602.

Another way to confirm the contamination level is to analyze *gtlike* results for this dataset. The likelihood analysis of the PSR J1907+0602 in 100 MeV-300 GeV yields a TS value of 22142,

while for Fermi J1913+0515 it yields a TS value of 54. We also produced model counts map of PSR J1907+0602 and Fermi J1913+0515 with *gtmodel* using the likelihood analysis. On the position of Fermi J1913+0515, 24 photons are expected to come from Fermi J1913+0515. In turn, 25 photons are expected to come from PSR J1907+0602 at the same position of interest.

Pulsar gating

To minimize the contamination from the nearby pulsar, we carried out our data analysis during the off-peak phases of PSR J1907+0602, following similar analyses^{44,45}. To define the off-peak interval, we divided the pulsed light curve into cells using the Bayesian Blocks algorithm described in ³⁹ (details can be found in ⁴⁶ and ⁴⁷). The off-peak interval is then defined as $\phi=0.0-0.136$ and $0.697-1.0$ (see Figure 4, right panel). Correspondingly, the prefactor parameters of all sources were scaled by 0.439 in the pulsar off-peak interval analysis, which is the width of the off-peak interval. The off-peak emission of PSR J1907+0602 was modelled with a power-law.

Off-peak analysis

During the off-peak of PSR J1907+0602, and assuming a power-law spectral shape, Fermi J1913+0515 is detected with a TS value of 39 ($\sim 5.9\sigma$) and a spectral index of $2.39 \pm 0.10_{stat} \pm 0.05_{sys}$, yielding an energy flux of $(1.25 \pm 0.24_{stat} \pm 0.39_{sys}) \times 10^{-11}$ erg cm⁻²s⁻¹. We also modelled Fermi J1913+0515 with a power law with an exponential cutoff ($dN/dE = N_0(E/E_0)^{-\Gamma} \exp(-E/E_0)$ cm⁻² s⁻¹ MeV⁻¹). However, the ΔTS ($\Delta TS = -2 \ln(L_{PL}/L_{CPL})$, where L_{CPL} and L_{PL} are the maximum

likelihood values for power-law models with and without a cutoff) between the two models is less than 9, which indicates that a cutoff is not significantly preferred. The extension of Fermi J1913+0515 was searched using *Fermipy* but no extension was found to be significant. For a further test, using *gtlike* we modelled Fermi J1913+0515 as a disk of different radius (from 0.1 to 0.5 degree with a step of 0.1 degree), all yielding a $TS_{ext} < 16$. No significant extension is detected. Assuming a power-law spectral shape, the likelihood analysis of the west excess resulted in a TS value of 15, a spectral index of $2.30 \pm 0.16_{stat} \pm 0.11_{sys}$, and an energy flux of $(0.75 \pm 0.25_{stat} \pm 0.41_{sys}) \times 10^{-11} \text{ erg cm}^{-2}\text{s}^{-1}$. Since this excess is not significantly detected (TS below the source detection threshold of 25), we do not consider its possible extension or the existence of a spectral cutoff. The TS map of SS 433 region is shown in Figure 1, top panel, together with the radio morphology from the Effelsberg 11 cm survey⁴⁸. The GeV spectral energy distribution (SED) of Fermi J1913+0515 and the west excess are shown in Figure 5.

Out of academic interest, and to compare with the former as well as with previous publications, we also carried out an analysis of the region without pulsar gating. As expected (see the discussion above regarding photon contamination) an extended/softer GeV excess is spatially associated with SS 433/W50 in this situation, similar to the results reported in¹⁹. Fermi J1913+0515 and the west excess can not be distinguished anymore. Fermi J1913+0515 would have a softer power-law index of 2.53 ± 0.03 . All of these result from the inclusion of photons that are not coming from the regions of interest, but from the contaminating pulsar, as demonstrated before.

Differences between the use of FL8Y and 4FGL

We note that Fermi J1913+0515 is associated with FL8Y J1913.3+0515 but that no 4FGL source is reported at this position. This is a result of a change in the diffuse model used in the 4FGL. Indeed, the FL8Y list has 5523 sources⁴⁹ while the 4FGL catalog has 5065 sources³³. The two catalogs used the same amount of data and software, but different interstellar emission model (gll_iem_v06 for FL8Y and gll_iem_v07 for 4FGL), also different energy range (100MeV–1TeV for FL8Y and 50MeV–1TeV for 4FGL) and a different threshold for using a curved spectral shape ($TS_{curve} > 16$ for FL8Y and $TS_{curve} > 9$ for 4FGL). The different interstellar emission model (higher at lower energies in the new model) used in each catalog is the main reason for the disappearance of sources. As stated in the 4FGL paper, changing the Galactic diffuse emission model from gll_iem_v06 to gll_iem_v07, even without changing the analysis or the data, the number of sources detected decreased by 10%.

Indeed, we carried out an analysis of 8 years P8R3 data in 50 MeV–1 TeV, which is the same time period and energy range used for the 4FGL. Using the 4FGL and assuming a power-law model, Fermi J1913+0515 is not significantly detected, with $TS=19$, which is consistent with the absence of a corresponding source in this list. However, using the 4FGL with the previous version of Galactic diffuse emission model (gll_iem_v06), Fermi J1913+0515 is again significantly detected with $TS=36$.

We have also checked our off-peak analysis presented in this paper using the FL8Y catalog.

Both Fermi J1913+0515 and the west excess are significantly detected with $TS=73$ and $TS=34$, respectively. Finally, we recall that above 1 GeV, the difference of results using FL8Y and 4FGL is minor and all the results included in this paper are consistent in both analysis.

Weighted light curve

Adopting the best-fit spectral-spatial model derived from the precessional phase-averaged analysis, we selected photons within a 3° -radius of SS 433 and calculated the probability that each event originated from Fermi J1913+0515 using *gtsrcprob*. For a better Point Spread Function (PSF) and less contamination from background sources, we only considered events above 1 GeV. Binning into 1-day intervals and correcting for the instrument exposure produced a light curve. We searched for the precessional periodic signal in the light curve between 145 and 175 days using the Lomb-Scargle periodogram method^{50,51}. Power spectra around the 162.250 days precession period were generated for the Fermi J1913+0515 exposure-corrected and exposure-uncorrected light curves using the Python packages *astropy* and *PyAstronomy*. No significant periodic signal was discovered in the uncorrected light curve. However, after the exposure correction is applied, a 160.88 ± 2.66 days period is detected with a single frequency significance of 3.6σ , consistent with the 162.250 days jet precession period. The single frequency significance was estimated using Python package *PyAstronomy*. “Standard” normalization method in Python package *astropy* was used. To calculate the false alarm probability and estimate how likely it is for the timing signal we detected to have an origin in noise, we implemented a bootstrap method. To construct the

simulated light curve, we keep the temporal coordinates the same as the actual light curve and assumed a Gaussian white noise for the flux. We computed Lomb-Scargle periodograms on 10^5 resampled, simulated light curves and derived the false alarm probability of the detected timing signal at our period of interest. All the sampled periods in the Lomb-Scargle periodogram have been considered in the bootstrap. Our results are shown in Figure 2 of the main text.

The Lomb-Scargle timing analysis has also been checked with different binning (e.g. 5 days, 7 days, 10 days) of the weighted light curve. The results are all consistent and do not depend on the weighted light curve binning. In addition, we note that the Fourier period resolution ($P^2/2T$, where P is the trial period and T is the observation interval) of our 10.5 years light curve at ~ 160 days is ~ 3.4 days. To infer the best period, the Fourier period resolution is usually oversampled by a factor of several, see e.g.,⁵². To obtain the results above, we oversampled it by a factor of ~ 4 , leading to a period resolution of ~ 0.8 days around 160 days. However, the evidence for the periodic signal at 160.88 ± 2.66 days do not depend on the period resolution adopted in the Lomb-Scargle periodogram: Other period resolutions around 160 days (e.g. ~ 1.0 , ~ 1.6 and ~ 3.4 days – i.e., with no oversampling) have been tested and all lead to consistent results.

Using the same light curve and a similar method, a search for the 13.082 days orbital periodic signal was carried out between 10 and 20 days, leading to no detections.

Likelihood analysis of the flux variation between precession phase 0.0–0.5 and 0.5–1.0

We adopted the precession period of 162.250 days from ¹⁰. The precessional phase zero (T_0) is set to the time of the largest separation of the moving emission lines in SS 433, JD 2443508.4098 (referred to as T_3 in ¹⁰). To estimate the significance of the flux variation between the precessional phase 0.0–0.5 and 0.5–1.0 described in the main text, we employed a likelihood analysis in 1–300 GeV. The two data sets of precessional phase 0.0–0.5 and 0.5–1.0 are jointly fitted using summed likelihood analysis. An additional co-spatial source with Fermi J1913+0515 is added for precession phase 0.0–0.5 to model any flux excess from that in the precession phase 0.5–1.0. With spectral index fixed at the value of Fermi J1913+0515 independently derived in precessional phase 0.0–0.5, the co-spatial source yields a TS value of 18 ($\sim 4.2\sigma$), and further demonstrates the significance of the flux difference between the two precessional phase bins. To further explore the trend of flux modulation, we show the precessional phase light curve of Fermi J1913+0515 in 1–300 GeV with a binning of 0.25 (Figure 3).

To calculate the significance of the flux deviation from a constant between precessional phase 0.0–0.5 and 0.5–1.0, the corresponding two data sets were fitted simultaneously using summed likelihood analysis. The spectral index of Fermi J1913+0515 was fixed to the value derived from precessional phase-averaged data. The analysis was carried out first with the normalization of Fermi J1913+0515 tied together through the two data set, and then repeated with it untied. The Δ TS between two maximum log-likelihood values is 12, which corresponds to a significance of 3.5σ and is consistent with the timing signal. The binning in the precessional phase, i.e., 0–0.5 and 0.5–1, is arbitrary and adopted a priori based on the ephemeris. Thus, only one trial is intro-

duced in the analysis. Because of the lower exposure time in smaller precessional phase bins, the corresponding uncertainties in the individual flux measurements grow, see Figure 3. However, as the latter Figure shows already, we tested a posteriori that the coarse variability trend is maintained even at smaller bins (e.g., even dividing the precessional phase in 10 bins, Figure 6).

As a consistency check, we carried out the same timing and precessional phase-related likelihood analysis in the 0.1-1 GeV band. No significant periodic signal is detected and no flux variation can be claimed. The ΔTS between maximum log-likelihood values of precessional phase 0.0–0.5 and 0.5–1.0 is 1.6.

The same check was further carried out above 1 GeV for the full dataset, i.e., without pulsar gating of PSR J1907+0602. A weak hint of a periodic signal at 161.93 ± 2.91 days is detected from Fermi J1913+0515 with a single-frequency significance of 2.7σ . The ΔTS between maximum log-likelihood values of precessional phase 0.0–0.5 and 0.5–1.0 is 8, indicating a flux deviation from a constant at 2.8σ level. The decreased significance of timing and flux variation are most likely due to the larger number of events that originate in PSR J1907+0602; its Poissonian flux fluctuation will smear the periodic flux variation from Fermi J1913+0515, which is much dimmer in comparison.

Stability of the timing signal

We also carried out a cumulative likelihood analysis during the precession phase 0.0–0.5 and

0.5–1.0 in 1–300 GeV. To allow for significant measurements along the evolution, we adopted a step of 8 precessional periods (1298 days), and show the evolution in time in Figure 7, top panel. The TS of Fermi J1913+0515 during the precessional phase 0.0–0.5 increases as observation time accumulates, while it stays almost unchanged during the precessional phase 0.5–1.0. As a result, the flux difference between the two precessional phase bins becomes more significant, providing additional credibility to the timing signal reported. Additionally, to explore further the stability of the timing signal, we employed the Weighted Wavelet Z-transform (WWZ⁵³). The 2D plane contour plotting for the WWZ power spectrum is shown in Figure 7, bottom panel. The timing signal at ~ 160 days is present along the 10.5 years observation time, but some intensity variation is apparent. Such variations may be an expected outcome in the scenario described if the injection is not constant, or the magnetic tube is not fixed in space.

Neutral atomic gas analysis

To compare the gamma-ray emission of SS 433 with the large-scale gas in the region, we used the 21 cm emission line of H I as a tracer of the neutral atomic gas. The Galactic ALFA H I (GALFA^{54,55}) survey data from the Arecibo Observatory 305 m-telescope was investigated. These data were first used in the report by⁸. The GALFA H I cube data have a grid spacing of 1 arcmin and a velocity channel separation of 0.184 km s^{-1} . Typical noise levels are 0.1 K rms of brightness temperature in an integrated velocity of 1 km s^{-1} .

Based on the Arecibo 21 cm H I data, we found an atomic gas excess coincident with Fermi

J1913+0515 at V_{LSR} 66km/s, which corresponds to a distance of $\sim 4.1 \pm 0.7$ kpc, consistent with that of SS 433^{20,56}. The enhancement is located at R.A. = 288.11° , decl.= 5.31° with a radius of ~ 15 arcmin (~ 20 pc at 4.6 kpc). The H I intensity of the main structure is ~ 1000 K km s⁻¹, leading to the total mass of $\sim 25000 M_\odot$. The volume-averaged density of the H I gas enhancement is estimated to be ~ 22 cm⁻³, assuming a spherical region of radius R_c . Given the relatively large grid spacing of the observations, the H I gas enhancement could be located in clumps or in a central cusp. The existence of clumps has often been found when clouds are observed at higher resolution in our Galaxy⁵⁷ and beyond⁵⁸. However, the low average density, on the other hand, make strong clumpiness, albeit in principle possible, unlikely⁵⁹.

X-ray data analysis

We have also analyzed two *ROSAT*/PSPC observations of the SS 433 region. *ROSAT*/PSPC ObsID RP400271A01 provides 20 ks exposure on the east lobe, whereas ObsID RP500058A02 provides 21 ks exposure on the west lobe of SS 433. The data were analyzed using xselect and ftools as suggested by the *ROSAT* data analysis manual⁶⁰. Exposure corrected X-ray images in 0.9–2.0 keV were produced and found to be consistent with⁶¹. The contour of east and west lobes in X-ray were shown in Figure 1, top panel.

GeV emission due to hadronic interactions?

In order to assess whether the GeV emission could be due to hadronic interactions, we con-

sidered a numerical solution of the (isotropic) diffusion equation –from an injection point up to a given distance– to compute the cosmic ray density. We then used the latter to compute the gamma-ray emission (similarly to what was done in ^{15,62}).

Provided that the interstellar cosmic-ray proton energy density in the region of SS 433 is the same as the locally detected one, we find that either in a continuous conversion of a fraction of the jet kinetic luminosity to cosmic rays, or in an impulsive cosmic-ray injection event of much shorter duration than the age of the jets, assumed here as $\sim 2 \times 10^4$ years, as in e.g., ⁶³ (albeit the argument would not be significantly changed in case this age is smaller, see ⁶⁴), the cosmic-ray density at the cloud could exceed the Galactic sea, generating gamma rays against the averaged proton density at a comparable level of flux to the one detected. The average level of gamma-ray flux we measure from Fermi J1913+0515 is equivalent to a luminosity of $10^{34} \text{ erg s}^{-1}$ at the SS 433 distance. To accommodate this luminosity via hadronic interactions, we need a total $W_p = 2.5 \times 10^{48} (L_\gamma / 10^{34} \text{ erg s}^{-1}) (n / 20 \text{ cm}^{-3})^{-1}$ erg in cosmic ray protons interacting with the atomic cloud. Protons might be accelerated at the terminal lobe, or come from the SS 433 equatorial outflow, and reach Fermi J1913+0515 through isotropic diffusion. The distance from east termination lobe or from the SS 433 central object to Fermi J1913+0515 are similar (See Figure 1). The kinetic power of both the jet and the equatorial outflow are also similar $\sim 10^{39} \text{ erg s}^{-1}$. Thus, in either scenario an accumulation of proton injection over ~ 100 yr is needed to supply the required proton energy, and consequently, any periodical signal due to injection will be smeared out.

Even if assuming that a sufficient cosmic-ray energy is injected in each single period to account for the observed gamma-ray flux, the difference of the arrival time to the cloud of cosmic rays between two consecutive injection events separated by a precessional period is small in comparison to the precessional period itself, such that many injections would still accumulate in the cloud, erasing the period signal produced by the arrival of fresh protons.

This situation is quantitatively exemplified in Figure 8 where we are purposely considering a mock period 500 times larger than the precessional one of SS 433 so that both, each individual instantaneous injection contains a larger amount of energy (equal to the kinetic power released in the period) and is more numerically tractable (given the need of considering only 100 periods to cover a significant age ~ 22000 yrs). In order to maximize even further the cosmic-ray luminosity at the cloud, this example will also purposely consider a high total luminosity of 3×10^{40} erg s $^{-1}$, of which 20% is assumed to end in cosmic rays at the injection point. We assume that the latter propagate isotropically in a medium with diffusion coefficient of 10^{28} cm 2 s $^{-1}$; we tested that changes in the latter will not modify conclusions. The first panel of Figure 8 shows the contributions to 10 GeV cosmic-ray (an example of an energy relevant for producing 1 GeV photons) at different distances from the injection point (around the separation between the cloud and SS 433) of 100 individual injection events, compared to the Galactic cosmic-ray sea -represented by the horizontal line. When the injection is very old, protons diffuse into a volume much larger than the region of interest. On the contrary, when it is too fresh (the last injection events, towards 100 in the x-axis of the figure), cosmic rays have not yet arrived to the region of interest. In both cases, the contribution

to the total cosmic-ray density at that energy is low. Instead, in intermediate times, each injection event can provide more 10 GeV cosmic rays than the Galactic sea. Note that this would not be the case should the real precessional period of SS 433 be considered (500 times smaller), i.e., the individual injections would be sub-dominant to the Galactic sea in that case although the general scenario would be maintained vis-a-vis. The second panel of Figure 8 shows the cosmic-ray density (at all energies): the green lines represent 10 individual injections separated (corresponding to 10, 20, 30... 100 in the x-axis of the first panel), whereas the violet line shows the sum of the contribution of all injection events. Similarly, the third panel of Figure 8 shows the hadronic gamma-ray emission at 1 GeV (obtained from a computation of a full spectral energy distribution, with the corresponding proton density) at different distances. To exemplify this further, we show in Figure 9 how the GeV gamma-ray flux evolves in time within the last ten precessional periods after an injection of ~ 22000 yrs. Again, we consider an impulsive periodical injection of cosmic rays and isotropic diffusion, but here we use with the real jet precessional period 162.25 days. The cloud is located 35 pc away from the cosmic-ray injection point. For typical ISM diffusion coefficients (i.e., $D_0 \sim 10^{28} \text{cm}^2 \text{s}^{-1}$), we cannot see any hint of the periodicity in gamma-ray flux, with a complete loss of the injection memory. We also examine the influence of the diffusion coefficient. A larger diffusion coefficient would in principle help to reveal the periodicity. However, we still cannot find any periodicity even with a diffusion coefficient up to $D_0 = 10^{30} \text{cm}^2 \text{s}^{-1}$. To focus on the temporal behavior, we normalize the fluxes in all three employed diffusion coefficients to the flux in the case of $D = 10^{28} \text{cm}^2 \text{s}^{-1}$. We can see the resulting gamma-ray flux decreases with increasing diffusion coefficient. So even if a larger diffusion coefficient, with which the periodicity can be present, is

somehow achieved, it would lead to an energy budget crisis to power the observed gamma-ray flux. Thus, this approach would be unable to explain the periodicity.

There are two ways of conceptually alleviating this situation. One can consider that cosmic rays interact with a gas enhancement in a small clump(s) or cusps of density. This helps in maintaining coherence of the signal when cosmic rays arrive periodically. One can also consider that anisotropic diffusion or streaming of cosmic rays along a flux tube is active, so as to ease the energetics: Differently to isotropic diffusion, streaming along a slim tube connecting the gas cloud and the particle injection point could in principle allow for most cosmic rays produced to arrive at the region of interest. In this way, if most protons injected within one precessional period arrive at the cloud clump, and quickly exit in half a period (i.e., ~ 80 days or 7×10^6 s, and a size of $R < c \times 80 \text{ days} \sim 0.07 \text{ pc}$ for the cloud clump), periodic coherence can in principle be maintained in gamma-rays. Using the mean free path for hadronic interactions $\text{mfp} \sim (n\sigma_{pp})^{-1}$, with n the clump density and σ_{pp} the hadronic cross section, we can see that assuming a clump density of about $\sim 10^4 \text{ cm}^{-3}$, the probability for them to interact is $\sim (1 - \exp(-(R/2)/\text{mfp})) \sim 10^{-4}$. If R , the clump size is about 0.07 pc (so that $R/2$ is about the light crossing time), with the assumed clump density the total mass in the cloud is quite small, $\sim 1M_{\odot}$; acceptable from the observational perspective (overall values of average density, mass, size, and angular resolution of observations). With this mass, considering that 10% of the power in the outflow (taken as $3 \times 10^{39} \text{ erg s}^{-1}$) goes into cosmic rays in each periodic illumination (i.e., assuming that 10% of the power in the outflow along half a precession period goes into cosmic rays), and the probability for them to interact, the

level of flux resulting from each injection event is comparable to observations. Also, note that each injection the magnetic flux can impact different regions of the cloud, what would explain some variability in the periodically produced signal. Despite how unlikely it might be to have a magnetic streaming connecting the injection point with the cloud, the low mass needed for the large energetics does not allow to rule this idea out, leaving it open for future studies.

Data Availability

The datasets generated during and/or analysed during the current study are available from the corresponding author on reasonable request.

References

1. Abeysekara, A. U. *et al.* Very-high-energy particle acceleration powered by the jets of the microquasar SS 433. *Nature* **562**, 82–85 (2018).
2. Fabrika, S. The jets and supercritical accretion disk in SS433. *Astrophysics and Space Physics Reviews* **12**, 1–152 (2004). [astro-ph/0603390](#).
3. Shklovskii, I. S. Mass Loss by SS433 and its Effect on the X-Ray and Radio Emission. *SvA* **25**, 315 (1981).
4. Fabian, A. C. & Rees, M. J. SS 433 - A double jet in action. *MNRAS* **187**, 13P–16P (1979).
5. Margon, B., Ford, H. C., Grandi, S. A. & Stone, R. P. S. Enormous periodic Doppler shifts in SS 433. *ApJ* **233**, L63–L68 (1979).
6. Middleton, M. J. *et al.* NuSTAR reveals the hidden nature of SS433. *arXiv e-prints* [arXiv:1810.10518](#) (2018). [1810.10518](#).
7. Dubner, G. M., Holdaway, M., Goss, W. M. & Mirabel, I. F. A High-Resolution Radio Study of the W50-SS 433 System and the Surrounding Medium. *AJ* **116**, 1842–1855 (1998).
8. Su, Y. *et al.* The Large-scale Interstellar Medium of SS 433/W50 Revisited. *Astrophys. J.* **863**, 103 (2018). [1807.03737](#).
9. Migliari, S., Fender, R. & Méndez, M. Iron Emission Lines from Extended X-ray Jets in SS 433: Reheating of Atomic Nuclei. *Science* **297**, 1673–1676 (2002). [astro-ph/0209131](#).

10. Davydov, V. V., Esipov, V. F. & Cherepashchuk, A. M. Spectroscopic monitoring of SS 433: A search for long-term variations of kinematic model parameters. *Astronomy Reports* **52**, 487–506 (2008).
11. Marshall, H. L., Canizares, C. R. & Schulz, N. S. The High-Resolution X-Ray Spectrum of SS 433 Using the Chandra HETGS. *Astrophys. J.* **564**, 941–952 (2002). [astro-ph/0108206](#).
12. Vermeulen, R. C., Schilizzi, R. T., Icke, V., Fejes, I. & Spencer, R. E. Evolving radio structure of the binary star SS433 at a resolution of 15 MARC S. *Nature* **328**, 309–313 (1987).
13. Safi-Harb, S. & Ögelman, H. ROSAT and ASCA Observations of W50 Associated with the Peculiar Source SS 433. *Astrophys. J.* **483**, 868–881 (1997).
14. Reynoso, M. M., Romero, G. E. & Christiansen, H. R. Production of gamma rays and neutrinos in the dark jets of the microquasar SS433. *MNRAS* **387**, 1745–1754 (2008). [0801.2903](#).
15. Bosch-Ramon, V., Aharonian, F. A. & Paredes, J. M. Electromagnetic radiation initiated by hadronic jets from microquasars in the ISM. *Astron. and Astrophys.* **432**, 609–618 (2005). [astro-ph/0411508](#).
16. Bordas, P., Yang, R., Kafexhiu, E. & Aharonian, F. Detection of Persistent Gamma-Ray Emission Toward SS433/W50. *Astrophys. J.* **807**, L8 (2015). [1411.7413](#).
17. Xing, Y., Wang, Z., Zhang, X., Chen, Y. & Jithesh, V. Fermi Observation of the Jets of the Microquasar SS 433. *Astrophys. J.* **872**, 25 (2019). [1811.09495](#).

18. Rasul, K., Chadwick, P. M., Graham, J. A. & Brown, A. M. Gamma-rays from SS433: evidence for periodicity. *MNRAS* **485**, 2970–2975 (2019). 1903.00299.
19. Sun, X. *et al.* Tentative evidence of spatially extended GeV emission from SS433/W50. *Astron. and Astrophys.* **626**, 113 (2019).
20. Collaboration, G. *et al.* The Gaia mission. *Astron. and Astrophys.* **595**, 1 (2016).
21. Aharonian, F. A. & Atoyan, A. M. Gamma rays from galactic sources with relativistic jets. *New Astronomy Reviews* **42**, 579–584 (1998).
22. Romero, G. E., Torres, D. F., Kaufman Bernadó, M. M. & Mirabel, I. F. Hadronic gamma-ray emission from windy microquasars. *Astron. and Astrophys.* **410**, L1–L4 (2003). astro-ph/0309123.
23. Reynoso, M. M., Christiansen, H. R. & Romero, G. E. Gamma-ray absorption in the microquasar SS433. *Astroparticle Physics* **28**, 565–572 (2008). 0707.1844.
24. Aartsen, M. G. *et al.* All-sky Search for Time-integrated Neutrino Emission from Astrophysical Sources with 7 yr of IceCube Data. *Astrophys. J.* **835**, 151 (2017). 1609.04981.
25. Reynoso, M. M. & Carulli, A. M. On the possibilities of high-energy neutrino production in the jets of microquasar SS433 in light of new observational data. *Astroparticle Physics* **109**, 25–32 (2019). 1902.03861.

26. Torres, D. F. & Reimer, A. Hadronic beam models for quasars and microquasars. *Astron. and Astrophys.* **528**, L2 (2011). 1102.0851.
27. MAGIC Collaboration *et al.* Constraints on particle acceleration in SS433/W50 from MAGIC and H.E.S.S. observations. *Astron. and Astrophys.* **612**, A14 (2018). 1707.03658.
28. Blundell, K. M. & Bowler, M. G. Symmetry in the Changing Jets of SS 433 and Its True Distance from Us. *ApJ* **616**, L159–L162 (2004). astro-ph/0410456.
29. Monceau-Baroux, R., Porth, O., Meliani, Z. & Keppens, R. The SS433 jet from subparsec to parsec scales. *Astron. and Astrophys.* **574**, A143 (2015).
30. Nava, L. & Gabici, S. Anisotropic cosmic ray diffusion and gamma-ray production close to supernova remnants, with an application to W28. *MNRAS* **429**, 1643–1651 (2013). 1211.1668.
31. Atwood, W. B. *et al.* The Large Area Telescope on the Fermi Gamma-Ray Space Telescope Mission. *Astrophys. J.* **697**, 1071–1102 (2009). 0902.1089.
32. URL <http://fermi.gsfc.nasa.gov/ssc/>.
33. collaboration, T. F.-L. Fermi Large Area Telescope Fourth Source Catalog (2019). arXiv:1902.10045.
34. URL <http://fermi.gsfc.nasa.gov/ssc/data/access/lat/BackgroundModels.html>.
35. Acero, F. *et al.* Fermi Large Area Telescope Third Source Catalog. *ApJS* **218**, 23 (2015). 1501.02003.

36. Wood, M. *et al.* Fermipy: An open-source Python package for analysis of Fermi-LAT Data. *35th International Cosmic Ray Conference. 10-20 July, 2017. Bexco, Busan, Korea, Proceedings of Science, Vol. 301, id.824* (2017). [arXiv:1707.09551](https://arxiv.org/abs/1707.09551).
37. Ackermann, M. *et al.* The Fermi Large Area Telescope on Orbit: Event Classification, Instrument Response Functions, and Calibration. *ApJS* **203**, 4 (2012). 1206.1896.
38. URL http://fermi.gsfc.nasa.gov/ssc/data/analysis/scitools/Aeff_Systematics.html.
39. Abdo, A. A. *et al.* The Second Fermi Large Area Telescope Catalog of Gamma-Ray Pulsars. *ApJS* **208**, 17 (2013). 1305.4385.
40. de Jager, O. C., Raubenheimer, B. C. & Swanepoel, J. W. H. A powerful test for weak periodic signals with unknown light curve shape in sparse data. *Astron. and Astrophys.* **221**, 180–190 (1989).
41. de Jager, O. C. & Büsching, I. The H-test probability distribution revisited: improved sensitivity. *Astron. and Astrophys.* **517**, L9 (2010). 1005.4867.
42. Hobbs, G. B., Edwards, R. T. & Manchester, R. N. TEMPO2, a new pulsar-timing package - I. An overview. *MNRAS* **369**, 655–672 (2006). [astro-ph/0603381](https://arxiv.org/abs/astro-ph/0603381).
43. Ray, P. S. *et al.* Precise γ -ray Timing and Radio Observations of 17 Fermi γ -ray Pulsars. *The Astrophysical Journal Supplement Series* **194**, 17 (2011). 1011.2468.

44. Abdo, A. A. *et al.* PSR J1907+0602: A Radio-Faint Gamma-Ray Pulsar Powering a Bright TeV Pulsar Wind Nebula. *Astrophys. J.* **711**, 64 (2010).
45. Li, J. *et al.* GeV Detection of HESS J0632+057. *Astrophys. J.* **846**, 169 (2017).
46. Jackson, B. *et al.* An algorithm for optimal partitioning of data on an interval. *IEEE Signal Processing Letters* **12**, 105 (2015).
47. Scargle, J. D., Norris, J. P., Jackson, B. & Chiang, J. Studies in Astronomical Time Series Analysis. VI. Bayesian Block Representations. *Astrophys. J.* **764**, 167 (2013).
48. Reich, W., Reich, P. & Fuerst, E. The Effelsberg 21 CM radio continuum survey of the Galactic plane between $L = 357$ deg and $L = 95.5$ deg. *A&AS* **83**, 539–568 (1990).
49. URL <https://fermi.gsfc.nasa.gov/ssc/data/access/lat/fl8y/>.
50. Lomb, N. R. Least-squares frequency analysis of unequally spaced data. *Astrophysics and Space Science* **39**, 447–462 (1976).
51. Scargle, J. D. Studies in astronomical time series analysis. II - Statistical aspects of spectral analysis of unevenly spaced data. *Astrophys. J.* **263**, 835–853 (1982).
52. Israel, G. The Basics of X-Ray Timing. *Urbino 2008: High Energy Astrophysics Summer School* (2008).
53. Foster, G. Wavelets for period analysis of unevenly sampled time series. *Astronomical Journal* **112**, 1709 (1996).

54. Peek, J. E. G. *et al.* The GALFA-HI Survey: Data Release 1. *ApJS* **194**, 20 (2011).
55. Peek, J. E. G. *et al.* The GALFA-HI Survey: Data Release 2. *ApJS* **234**, 2 (2018).
56. Reid, M. J. *et al.* Trigonometric Parallaxes of High Mass Star Forming Regions: The Structure and Kinematics of the Milky Way. *Astrophys. J.* **783**, 130 (2014).
57. Heyer, M. & Dame, T. M. Molecular Clouds in the Milky Way. *A&AR* **53**, 583–629 (2015).
58. Fukui, Y. & Kawamura, A. Molecular Clouds in Nearby Galaxies. *A&AR* **48**, 547–580 (2010).
59. Bergin, E. A. & Tafalla, M. Cold Dark Clouds: The Initial Conditions for Star Formation. *A&AR* **45**, 339 (2007).
60. URL https://heasarc.gsfc.nasa.gov/docs/rosat/ros_xselect_guide/.
61. Brinkmann, W., Aschenbach, B. & Kawai, N. ROSAT observations of the W 50/SS 433 system. *Astron. and Astrophys.* **312**, 306 (1996).
62. Aharonian, F. A. & Atoyan, A. M. On the emissivity of π^0 -decay gamma radiation in the vicinity of accelerators of galactic cosmic rays. *Astron. and Astrophys.* **309**, 917–928 (1996).
63. Panferov, A. A. Jets of SS 433 on scales of dozens of parsecs. *Astron. and Astrophys.* **599**, A77 (2017). 1607.02043.
64. Goodall, P. T., Blundell, K. M. & Bell Burnell, S. J. Probing the history of SS 433’s jet kinematics via decade-resolution radio observations of W 50. *MNRAS* **414**, 2828–2837 (2011). 1103.5658.

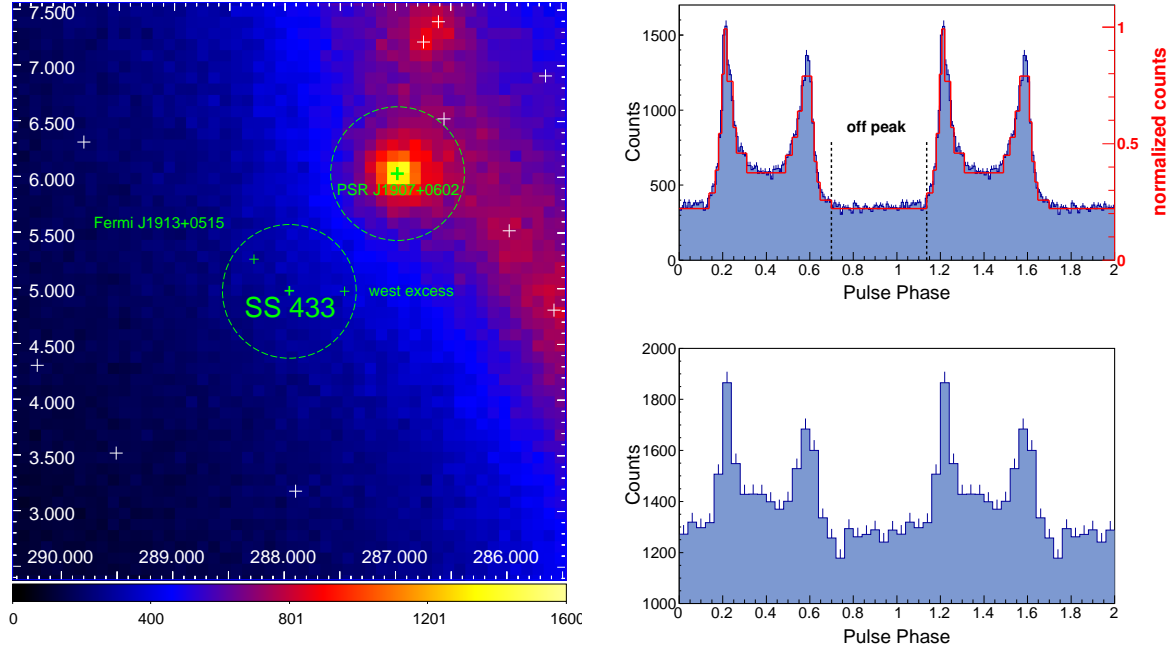


Figure 4: Gamma-ray pulsar PSR J1907+0602's contamination on SS 433 region. **Left:** 100 MeV – 300 GeV counts map of the *Fermi*-LAT field of the SS 433 region. The microquasar itself is noted with a bold cross. The fitted position of Fermi J1913+0515 and west excess are shown with green crosses. The X- and Y-axes are R.A. and decl. referenced at J2000. The regions used to produce pulse profiles are shown with dotted circles. **Right-top:** Folded pulse profile of PSR J1907+0602 above 300 MeV with an ROI of 0.6° . Two rotational pulse periods are shown, with a resolution of 100 phase bins per period. The Bayesian block decomposition is shown by red lines. The off-peak interval ($\phi=0.697\text{--}1.136$) is defined by black dotted lines. **Right bottom:** Folded pulse profile of the photons centered on SS 433 with a radius of 0.6° above 100 MeV, using the ephemeris of PSR J1907+0602. Two rotational pulse periods are shown, with a resolution of 25 phase bins per period.

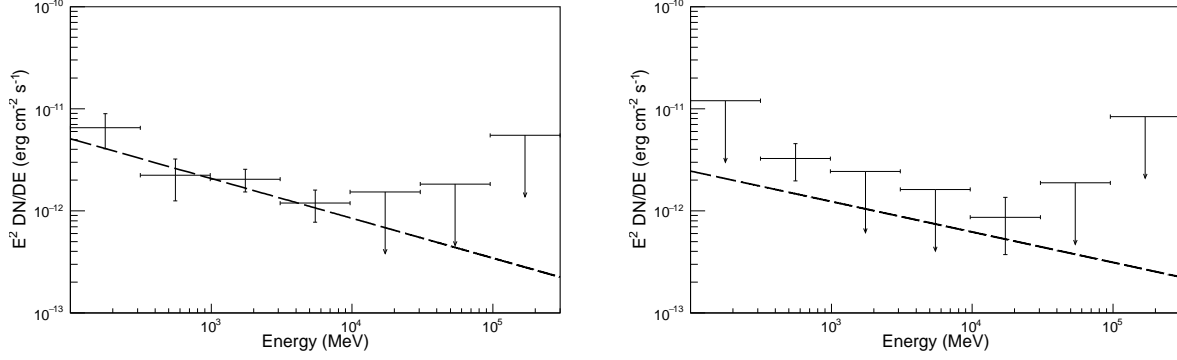


Figure 5: *Fermi*-LAT spectra of Fermi J1913+0515 (left) and the west excess (right). The maximum likelihood model (power law) fitted with *gtlike* is shown with a dashed line.

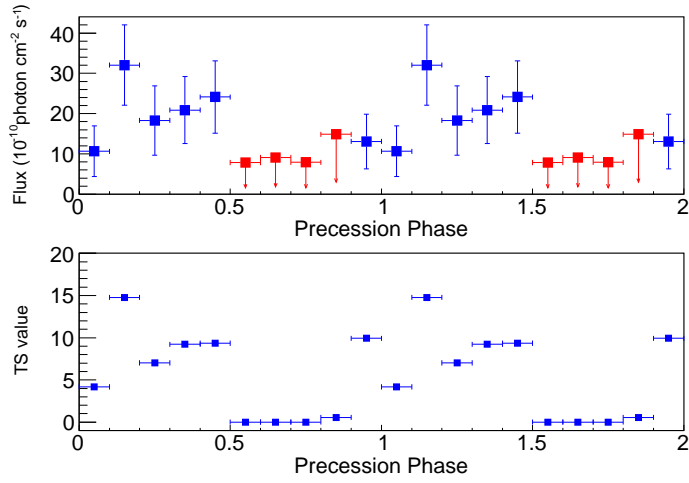


Figure 6: Precessional phase light curve (top) and TS values (bottom) of Fermi J1913+0515 in 1-300 GeV with a binning of 0.1. The upper limits are at the 95% confidence level.

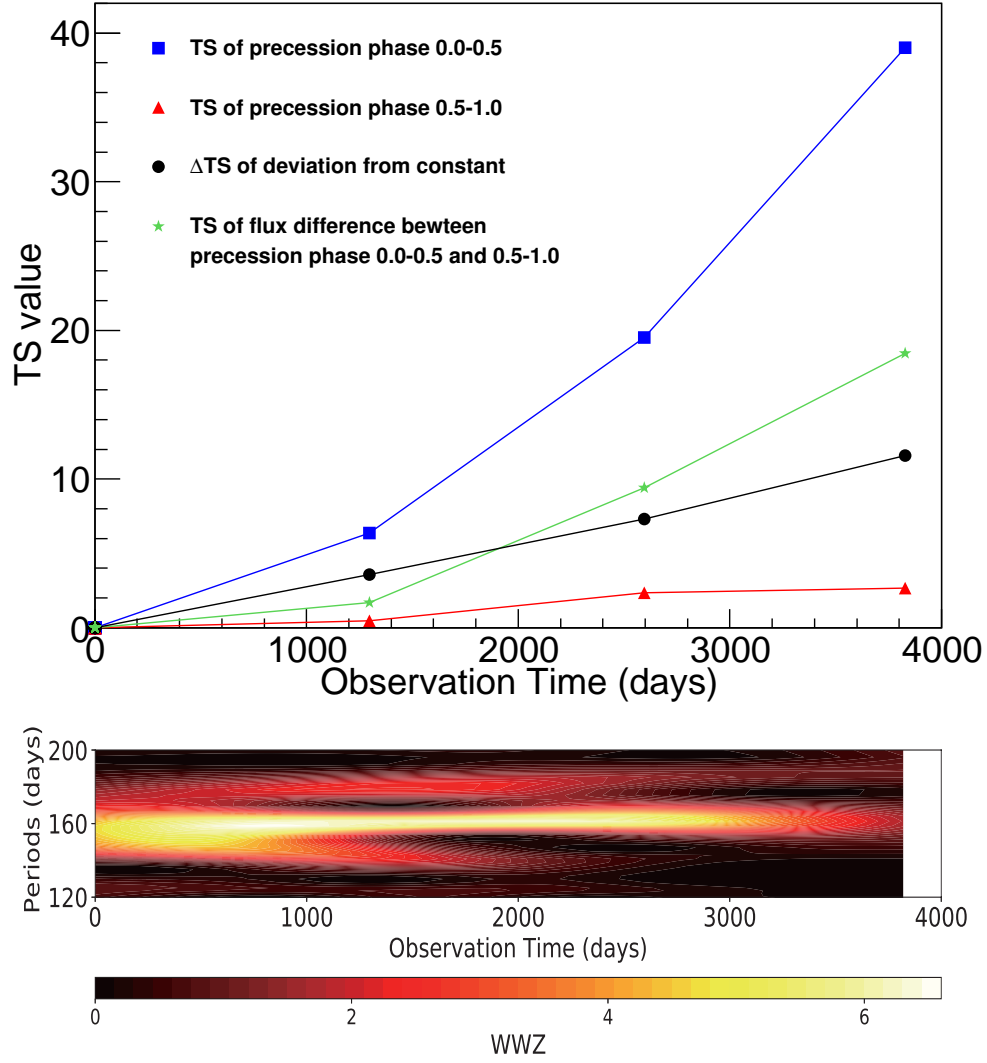


Figure 7: Top: cumulative likelihood analysis during precession phase 0.0–0.5 and 0.5–1.0. the TS of Fermi J1913+0515, Δ TS of the flux deviation from a constant and TS of the flux difference between two precessional phase bins are shown with different color and marker. Bottom: 2D plane contour plotting for the WWZ power spectrum.

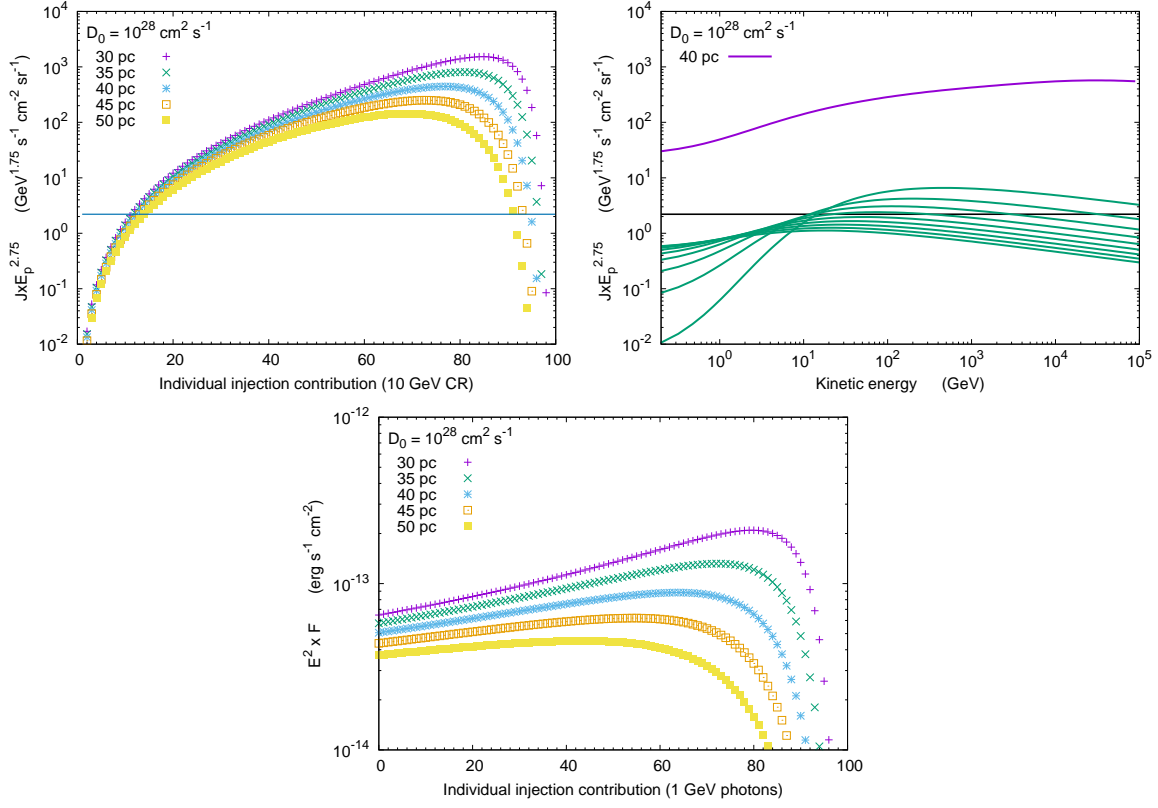


Figure 8: Examples of simulations for a periodic, instantaneous injection of protons. Details are described in the text.

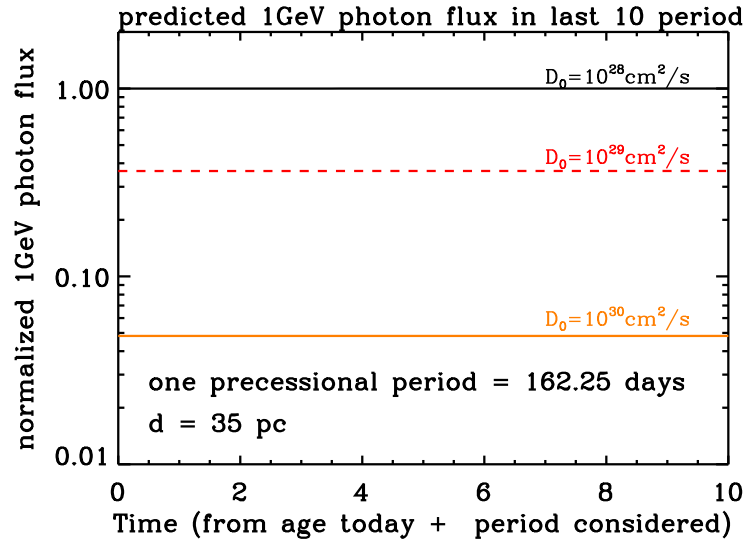


Figure 9: Predicted 1 GeV gamma-ray flux in the last ten precessional periods computed with different diffusion coefficient. Details are described in the text.